The Impact of High-Productivity Processing on the Fatigue Failure of an Additive Manufactured Superalloy HAYNES 282

Advanced Engineering Materials

ADVANCED ENGINEERING MATERIALS
www.aem-journal.com

RESEARCH ARTICLE OPEN ACCESS

The Impact of High-Productivity Processing on the Fatigue Failure of an Additive Manufactured Superalloy HAYNES 282

Abdul Shaafi Shaikh[1,2] | Ahmed Fardan[1] | Tatiana Mishurova[3] | Eduard Hryha[1]

[1]Department of Industrial and Materials Science, Chalmers University of Technology, Gothenburg, Sweden | [2]Electro Optical Systems Finland Oy, Turku, Finland | [3]Bundesanstalt für Materialforschung und -prüfung, Berlin, Germany

Correspondence: Abdul Shaafi Shaikh (abdulsh@chalmers.se)

Received: 5 August 2025 | **Revised:** 24 October 2025 | **Accepted:** 16 January 2026

Keywords: additive manufacturing | computed tomography | fatigue | fractography | powder bed fusion – laser beam | superalloy

ABSTRACT

The elevated temperature low cycle fatigue life of additively manufactured HAYNES 282 superalloy from conventional 40 µm layer thickness process parameters was compared with that of high-productivity 80 µm layer thickness process parameters. Wrought 282 alloy was also tested in parallel for comparison. The 40 µm process parameters produced fatigue life between 1400 and 1700 cycles to failure, the 80 µm process parameter specimens failed after ≈1200 cycles, and the wrought alloy reached 1350 cycles to failure. Microstructure investigations did not reveal systematic differences in phase constituents or grain structure between 40 and 80 µm processed 282 alloy. While both process parameters produced porosity of less than 0.05% by volume, high-resolution X-ray computed tomography showed the occurrence of large aspect ratio lack of fusion defects in the 80 µm material. These defects were also identified on fracture surfaces and could be related to the accelerated initiation and propagation of cracks, especially when oriented perpendicular to the load axis in samples built parallel to the building direction. The results emphasize the criticality of seemingly minor variations in defect characteristics on performance in cyclic loading conditions for high strength alloys.

1 | Introduction

Additive manufacturing (AM) by powder bed fusion-laser beam (PBF-LB) is an increasingly important manufacturing method for Ni-base superalloy components in the energy and aerospace industries. Superalloy components in such industries are subject to extreme temperature and stress conditions, including different forms of cyclic loading. Fatigue performance of PBF-LB manufactured superalloys is therefore an important subject of investigation to enable safe adoption of AM in critical components.

Studies on fatigue of AM superalloys have shown these materials to be either similar in properties [1, 2], poorer in fatigue life [3, 4], or in some cases better in performance [5, 6] compared to their conventionally manufactured counterparts. Fatigue properties have been found to be dependent on the AM processing, the heat treatment, and the specific fatigue testing conditions [7, 8]. The fatigue resistance of conventionally manufactured superalloys typically depends on the extent and nature of defects and inclusions present in the material, but also on microstructure, deformation behavior, and oxidation behavior [9, 10]. However, AM technology is particularly sensitive to defect formation due to its layer-wise nature, and many instances of premature failure of AM structures have been linked to residual porosity [7]. Defects are known to be especially influential when applied strain ranges are high [11]. Apart from defects, the fatigue performance can also be influenced by grain size, microstructure, and surface condition, which can vary widely for AM materials [7, 8, 12].

Note: "Haynes" and "282" are registered trademarks of Haynes International, Inc, Kokomo, Indiana, USA.

Defects and porosity in PBF-LB are primarily controlled by process parameters, particularly when hardware and material feedstock are held constant. However, the process parameters also have a strong impact on productivity of the manufacturing process [13]. In particular, layer thickness has an influence on the throughput and therefore the cost of AM parts, showing potential to double the build rate when layer thickness is increased from 40 to 80 μm [14]. While conventional layer thicknesses for metal PBF-LB are in the range of 20 to 50 μm, there is an increased interest in industry towards enhancing build rates by the use of high-productivity process parameters, which are characterized by higher layer thicknesses in the range of 80 μm and above [15]. These high-productivity process parameters have been shown to produce mechanical performance comparable with conventional parameters, e.g., Leicht et al. showed that PBF-LB processing of 316L stainless steel in 80 μm layers could achieve nominal densities in excess of 99.9%, and tensile properties comparable with the conventional 20 μm layer thickness process parameters [16]. Paradise et al. performed room temperature mechanical tests of PBF-LB IN718 manufactured using 60 μm and 80 μm layer thicknesses, concluding that properties after postbuild heat treatment were comparable to that of conventional IN718 [17]. On the other hand, high-productivity process parameters have also been shown to be more susceptible to defect formation due to large melt track sizes and reduced remelting of underlying material, and little data is available on the comparative mechanical performance of conventional and high-productivity PBF-LB processed materials when exposed to elevated temperature or cyclic loading. Further, it is known that static tensile properties are generally less sensitive to defects than fatigue properties [18], which motivates the investigation of cyclic loading for high-productivity processed materials by PBF-LB.

The current investigation aims to examine the fatigue performance of a Ni-base superalloy HAYNES 282 (henceforth referred to as 282 alloy, note that 'Haynes' and '282' are registered trademarks of Haynes International, Inc, Kokomo, Indiana, USA.) manufactured in PBF-LB by conventional and high-productivity process parameters. 282 alloy is a relatively new superalloy which has been shown to be well processable in AM [19], while also producing mechanical performance on par with conventional forms [20, 21]. While fatigue performance of the alloy in conventional forms has been extensively investigated [22–26], the fatigue performance of the PBF-LB version of the alloy, especially at elevated temperatures, is not yet widely reported. The objectives of this article are, therefore, to understand the effect of microstructure and defects from PBF-LB processing, including those from high-productivity parameters, on elevated temperature fatigue of 282 alloy processed by PBF-LB.

2 | Materials and Methods

Samples for material testing were manufactured using an EOS M290 system, which has a building platform size of 250 mm × 250 mm. The process parameter set titled 'Haynes282_040_080_CoreM291' from EOS GmbH was utilized, which includes a 40 μm layer thickness exposure set as well as an 80 μm layer thickness exposure set, developed by the principal author. Specifically, the exposure set 'EOS_DirectPart' with volumetric energy density E_v of 56 J/mm^3 was utilized for conventional 40 μm layer thickness processing, while the exposure set 'EOS_DirectPart_Fast' with E_v of 39 J/mm^3 was used for high-productivity 80 μm layer thickness processing. The standard configuration of hardware recommended by the manufacturer was utilized, i.e., high-speed steel recoater, Ar shielding gas, and steel building platform. The powder feedstock was EOS NickelAlloy HAYNES 282 and the chemical composition of the powder is given in the Table 1. The powder was not in virgin condition but had previously been used for building test parts and subsequently sieved with a 63 μm sieve according to recommended practice. Parts in 40 and 80 μm layer thickness were manufactured within the same build job. Samples manufactured with the different layer thickness parameters will henceforth be called '40 μm' or '80 μm' for ease of reference.

To demonstrate the difference in productivity between the 40 and 80 μm process parameters, build times were simulated using EOSPRINT 2.17 using example geometries. Figure 1 shows the build layout, which featured six gas turbine ring segments and four tensile bar blanks. Total building time using 40 μm was 51 h and 21 mins, whereas building time for 80 μm was 29 h and 26 mins, i.e., PBF-LB building time was predicted to be ≈43% less when using high-productivity processing compared to conventional. Further details including recoating and exposure times can be found in Table 2.

Samples for mechanical testing were built as cylinders of 15 mm diameter and 80 mm length, oriented either parallel or perpendicular to the building direction (BD). Samples built parallel and perpendicular to the BD will henceforth be referred to as 'vertical' and 'horizontal' samples. Metallographic analysis samples were manufactured as 15 mm cubes. Samples for X-ray computed tomography (XCT) scanning were manufactured as 6 mm diameter cylinders with 50 mm height in the vertical orientation.

After PBF-LB processing the manufactured test parts were removed from the building platform by a bandsaw and heat treated in a TAV H4S type industrial vacuum furnace. Pressurized Ar gas was used for the cooling steps. The heat treatment regime, which has previously been shown to improve elevated temperature ductility and reduce anisotropy in PBF-LB 282 alloy [21], consisted of the following three steps: (1) a solution treatment of 1250°C for 2 h followed by gas quenching at ≈100°C/min; (2) first ageing at 1010°C for 2 h with forced gas cooling at ≈20°C/min; and (3) second ageing at 788°C for 8 h with forced gas cooling at ≈20°C/min.

Wrought superalloys are often considered a benchmark for properties when developing AM superalloys, motivating the comparison of fatigue life between wrought and PBF-LB 282 alloy. Since fatigue testing results can vary depending on the precise conditions of testing, wrought 282 alloy was also tested in parallel to

TABLE 1 | Chemical composition of the powder alloy in wt.%.

Ni	Cr	Co	Mo	Ti	Al	C	B	O	N	S	Fe	Si
Balance	19.4	10.3	8.4	2.1	1.6	0.04	0.007	0.018	0.009	0.0018	0.09	0.05

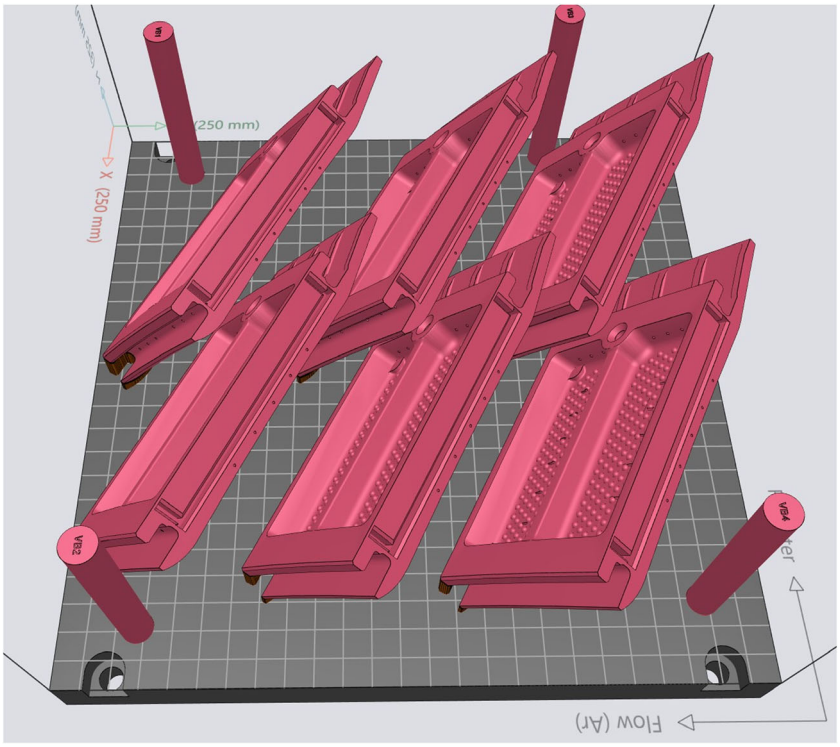

FIGURE 1 | Geometries including gas turbine ring segments and tensile bars blanks used for simulating PBF-LB building time with conventional and high-productivity process parameters.

TABLE 2 | Comparison of PBF-LB processing times between 40 and 80 µm processing parameters for the example build layout in Figure 1.

Process parameter	Exposure time, hh:mm	Recoating time, hh:mm	Total building time, hh:mm
40 µm	46:14	5:07	51:21
80 µm	26:52	2:33	29:26

PBF-LB 282 alloy to enable a fair comparison. The wrought alloy was obtained from Haynes International Inc as a rolled plate of 15.9 mm thickness and the test specimens were extracted in the long transverse orientation. Note that wrought material was subjected to the same ageing heat treatment as the PBF-LB alloy, but no solutionizing was done, as the material was received in mill annealed condition, which is equivalent to the solution treated condition of the PBF-LB alloy [27].

Specimens for low cycle fatigue (LCF) tests were machined, ground, and longitudinally polished to a cylindrical dog-bone shape with a 5.08 mm gauge diameter and 19.05 mm parallel length. LCF tests were performed in strain control according to ASTM E606−21 at 760°C, with a triangular waveform, frequency of 20 cycles per minute, total strain range of 1.0%, and stress ratio of −1 (fully reversed tension-compression loading). Two specimens were tested per condition and orientation – see Table S1 for a complete list of tests.

For the microstructure analysis, cube-shaped samples were printed and cut parallel to the BD (ZY section) and perpendicular to the BD (XY section) and mounted in Struers' Polyfast conductive resin. This was followed by standard metallographic preparation with SiC papers and various cloths with progressively finer diamond paste down to a 1 µm finish. Samples for the purpose of microstructure observation were then electrolytically etched at 6 V with 10 wt.% oxalic acid. For electron backscattered diffraction (EBSD) analysis the samples were not etched but further polished with colloidal silica until grain relief was optically visible. Metallographic samples were prepared in duplicate per condition and orientation, with one sample used for EBSD analysis and the other for general microstructure analysis.

General microstructure and fracture surface observations were made on a Zeiss GeminiSEM 450 scanning electron microscope (SEM). For EBSD analysis a LEO Gemini 1550 SEM was used with a Nordlys II detector. A step size of 3 µm was used for pattern acquisition, and the EBSD data was processed and analyzed with the Oxford AztecCrystal software, considering a 10° misorientation angle for grain determination.

XCT measurements were performed on a General Electric v|tome|x L 300 scanner, with one specimen being analyzed for 40 µm and one specimen for 80 µm. A single scan consisted of 2500 projections, using an acquisition time of 3 s for each projection. The tube voltage used was 160 kV with a current of 60 µA reaching a voxel size of 3 μm^3. Fiji ImageJ and AvizoFire 9.4 were used for data gathering and processing. To avoid false segmentation, only defects with a minimum volume of 5 voxels were considered in the analysis. Thus, defects with minimum equivalent diameter of around 7 µm were detected.

3 | Results and Discussion

The results in the following section are presented in order of investigation. The LCF results are described first, followed by

characterization of the material conditions, focusing on variables anticipated to influence fatigue behavior, particularly microstructural features such as phase constitution, grain structure, and porosity. Subsequently, fractographic and metallographic analyses of failed LCF specimens are presented to establish a link between material condition and the trends observed in the LCF tests.

3.1 | Low Cycle Fatigue

All LCF tests were run until specimen failure. The number of cycles to failure N_f are plotted against the sample condition (processing parameter and orientation) and shown in Figure 2. As two samples were tested per condition, the average is plotted along with error bars indicating the maximum and minimum test result. Further details of the tests, including cycles to initiation N_i, defined by 10% load drop from maximum load, are shown in Table S1. All samples failed within the range of 1000–2000 cycles. The longest fatigue life averaged over two samples was shown by the 40 µm vertical samples, followed by the 40 µm horizontal samples. The 80 µm vertical samples showed the lowest N_f of all, and one sample notably showed no difference between N_i and N_f. The wrought 282 alloy showed the largest difference in N_f between the 2 tested samples, though the average N_f was 1343 cycles.

While the difference between 40 and 80 µm parameters is not large considering the typical scatter of LCF testing results [28, 29], the trend over all tested samples suggests that 40 µm PBF-LB 282 alloy shows longer fatigue life than 80 µm under the described test conditions. The fatigue life of Ni-base superalloys is influenced by several material characteristics, with the most relevant factors being grain size, microstructure, and defects [9, 30]. Each of these factors was analyzed to determine their effect on fatigue life and are shown in sections 3.2 to 3.4 below. Other known influences such as surface condition were the same for all tested samples, and are therefore not considered as a variable in the upcoming analysis. Note that the monotonic

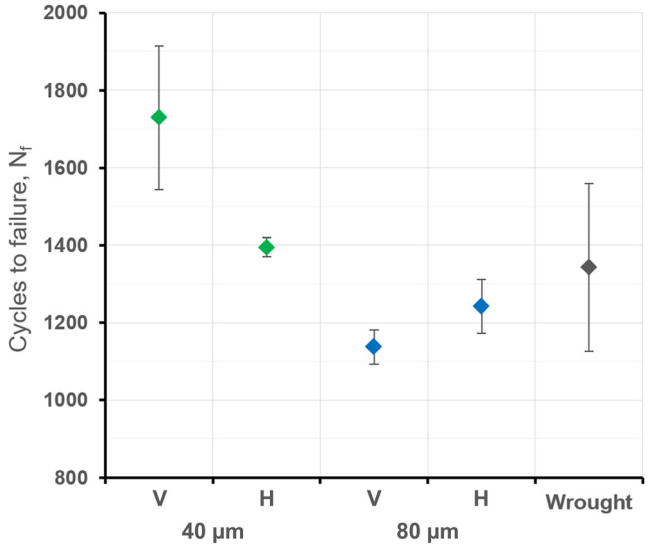

FIGURE 2 | Cycles to failure for PBF-LB 282 alloy, for two process parameters and orientations. Testing in strain control at 760 °C and 1% total strain range. Results for Wrought 282 alloy are also shown.

tensile strength and ductility of the 40 and 80 µm 282 alloy at 760°C are very similar (see Table 3) and this property is therefore not considered to be a contributing factor. The hardening and softening behavior for all samples was also found to be similar to that described by Buckson et al. [26] for wrought 282 alloy, and is not discussed in detail in this text.

3.2 | Grain Size

Maps from EBSD analysis depicting grain structure of the 40 and 80 µm PBF-LB 282 alloy in planes parallel and perpendicular to the BD are shown in Figure 3. All analyzed samples showed a grain structure coarser than typically found in the as-built condition of PBF-LB 282 alloy [19, 20, 31–34]. The high solution treatment temperature of 1250°C promotes grain growth in the microstructure [20, 21, 32]. Frequent twin boundaries were also noted in the microstructure, and no pronounced texture was observed. The grain sizes in terms of equivalent circle diameter were extracted from the EBSD maps and plotted as distributions on boxplots seen in Figure 4. Note that grain sizes were calculated from parent grains, excluding twin boundaries.

The measurement results in Figure 4 suggest that the 40 and 80 µm conditions exhibited generally similar grain size. This is evidenced by the similar values of mean grain size, and of P25 and P75 grain sizes for all distributions. Certain minor variations were noted, including a larger median (P50) grain size for the 40 µm sample in the plane perpendicular to the BD, however this is likely to be a feature of the specific region measured by EBSD, as seen from the exceptionally large grain at the bottom right of Figure 3b. No major systematic differences were observed in grain size or morphology between the different conditions.

3.3 | Microstructure

The 40 and 80 µm 282 alloy both exhibit a typical γ-γ' microstructure, with carbides at grain boundaries, as shown in Figure 5. Grain boundary carbides were spaced closely together along with grain boundary γ', forming nearly continuous chains. This configuration of grain boundary phases has been reported previously for 282 alloy [21, 27], and detailed analysis of the grain boundary carbides found elsewhere [34–36] suggests that these are expected to Cr-rich $M_{23}C_6$ carbides along with Mo-rich M_6C carbides. Small intragranular carbides were also observed within grains. The fine intragranular γ' appeared spherical in morphology, and measurements by image analysis showed very similar size for both conditions. In the 40 µm 282 alloy the γ' was 38 ± 12 nm in diameter, and in the 80 µm 282 alloy the γ' was 42 ± 8 nm in diameter. Such a small difference in precipitate size is likely related to variations in the cooling rates from ageing steps [37] and thus not considered to be consequential for the mechanical performance of the alloy.

3.4 | Porosity

Analysis of the porosity by XCT revealed a major difference between the 40 and 80 µm 282 alloy conditions. A 3D rendering of the XCT reconstructions is presented in Figure 6, where red coloring indicates the absence of dense material, i.e., porosity/defects. As can be seen from the reconstruction, the 40 µm

TABLE 3 | Results of tensile testing at 760 °C for 40 and 80 µm alloy 282. Tensile testing on 6 mm diameter cylindrical samples according to ISO 6892–2 using strain rate of 2.5×10^{-4} s^{-1} until yield followed by 1.4×10^{-3} s^{-1} to failure.

Condition	Orientation	Yield strength, MPa	Ultimate tensile strength, MPa	Elongation after fracture 4D, %	Reduction in area, %
40 µm	Vertical	597	835	31.5	34
	Horizontal	620	844	26.5	29
80 µm	Vertical	592	834	29.5	33
	Horizontal	616	853	26.5	29

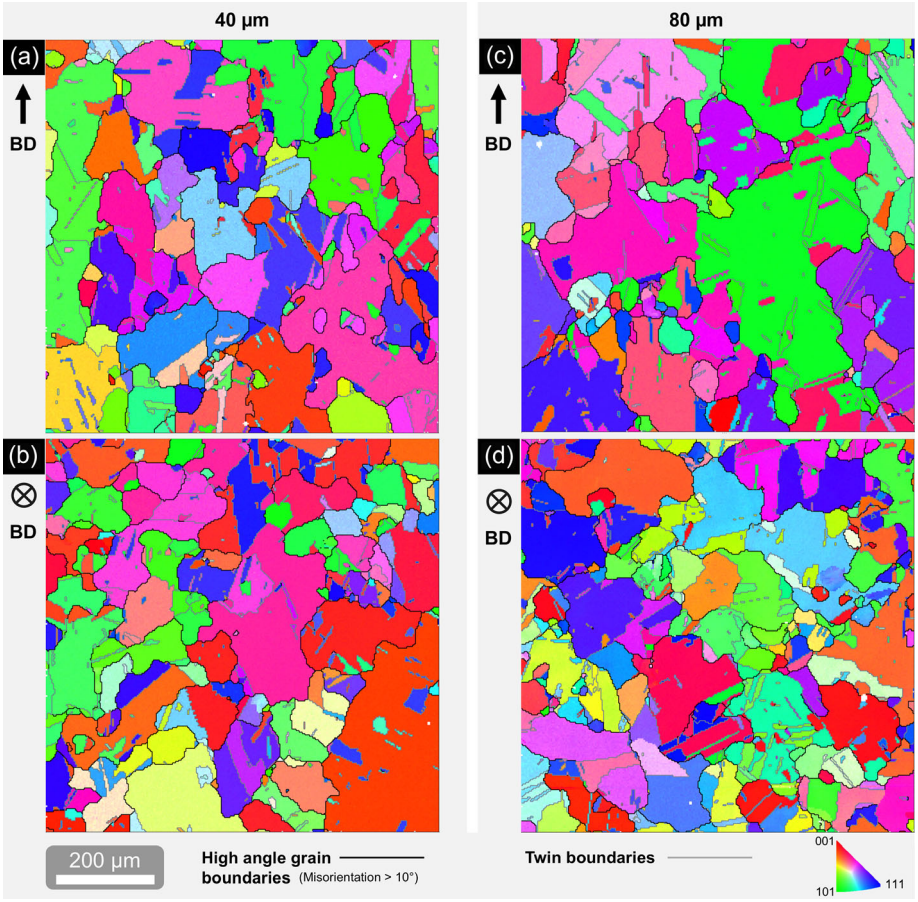

FIGURE 3 | EBSD orientation maps in inverse pole figure (IPF) representation for (a) and (b) 40 µm 282 alloy; and (c) and (d) 80 µm 282 alloy in cross-sections parallel and perpendicular to the BD. IPF coloring is along the BD.

sample showed small spherical pores, whereas the 80 µm sample showed small spherical pores as well as larger pores with a higher aspect ratio. The insets in Figure 6 show magnified versions of typical pores found in the samples. The large pores found in the 80 µm sample tend to have their major dimension oriented perpendicular to the build direction, which suggests that these are lack of fusion defects [8, 38]. The volume fraction of porosity was calculated to be 0.004% for the 40 µm sample and 0.036% for the 80 µm sample. While both these values are small in absolute terms, the difference in porosity between the process parameters is significant.

A quantitative representation of the comparative sphericity and size of the porosity distributions is shown in Figure 7. The 40 µm sample had pores which were no larger than 40 µm (in equivalent spherical diameter) and tended to have high sphericity. Such pores are also present in the 80 µm sample, however, the distribution for the 80 µm sample was extended towards large defect sizes, with equivalent spherical diameters up to 130 µm. Note that a low sphericity for a pore implies that the maximum dimension of the defect is much larger than the equivalent spherical diameter. For the 80 µm sample the larger pores were also less spherical, further supporting the understanding that these are lack of fusion defects [30]. The increased propensity to porosity and lack of fusion defects in larger layer thickness PBF-LB processing is consistent with the literature and has been correlated to increased melt pool instability, more spatter generation, and reduced remelting of underlying material when layer thickness is high [14, 16, 39, 40]. Further detailed analysis of the cause of porosity and optimization of PBF-LB process parameters is beyond the scope of the present investigation.

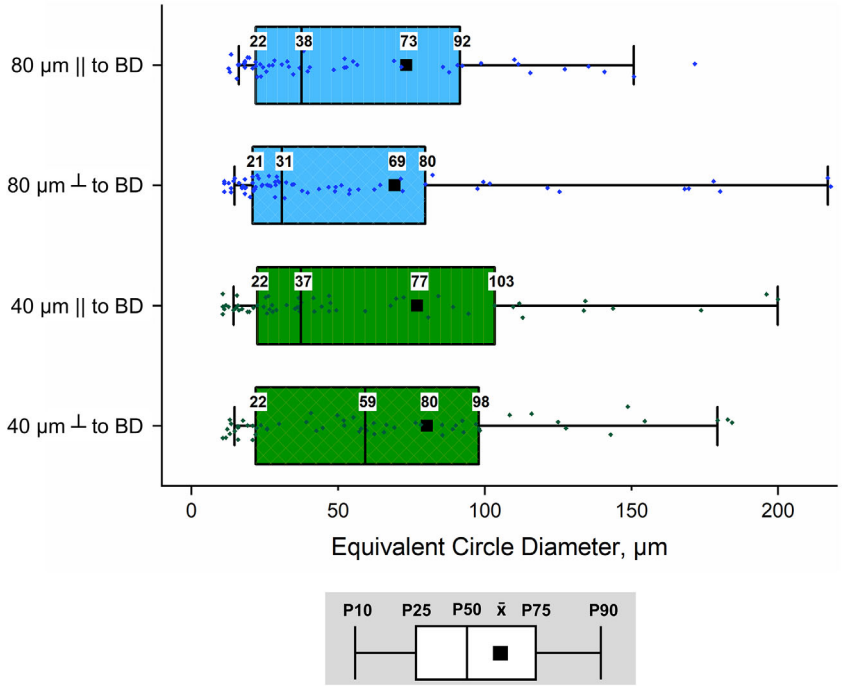

FIGURE 4 | Box and whisker plots representing the distribution of equivalent circle diameter grain sizes from EBSD measurements of 40 and 80 µm 282 alloy from cross sections parallel and perpendicular to BD. The 10th, 25th, 50th, 75th, and 90th percentiles of the distribution are represented by P10, P25, P50, P75, and P90, respectively. $\bar{x}$ represents the mean value.

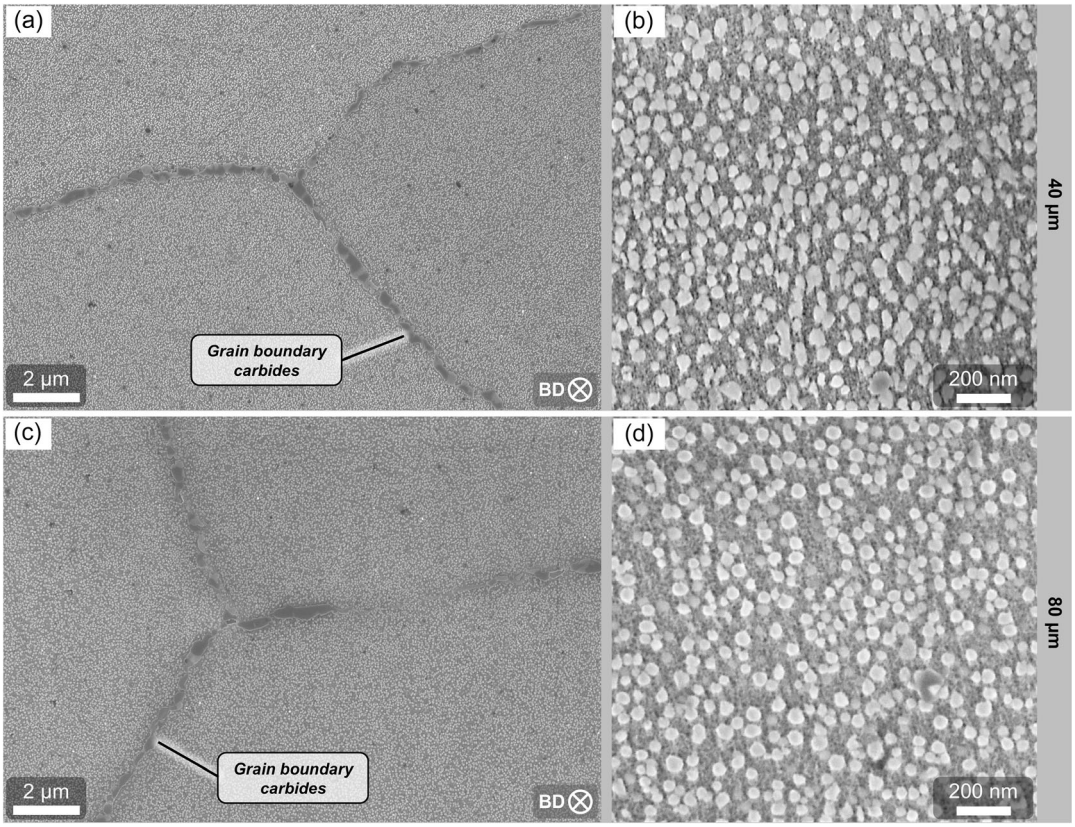

FIGURE 5 | SEM micrographs with InLens detector showing the microstructure of (a) and (b) 40 µm 282 alloy; and (c) and (d) 80 µm 282 alloy. All micrographs are of cross-sections perpendicular to the BD.

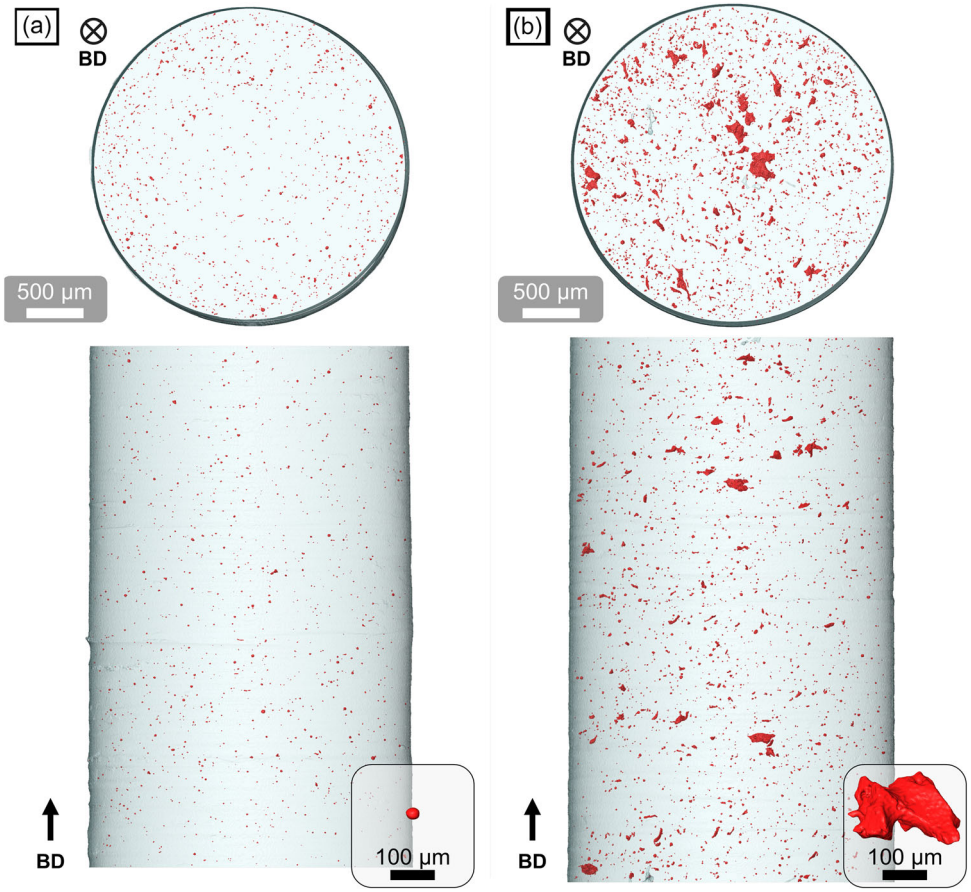

FIGURE 6 | 3D rendering of samples and porosity obtained by XCT in (a) 40 µm 282 alloy; and (b) 80 µm 282 alloy. Insets show isolated defects from each condition.

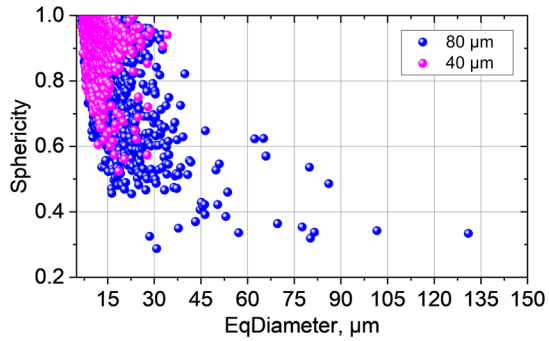

FIGURE 7 | Distribution of defects detected by XCT in 40 and 80 µm 282 alloy in terms of sphericity and equivalent spherical diameter.

The XCT analysis showed a clear difference in porosity volume fraction, size, and morphology between 40 and 80 µm samples. The sharper and larger defects in the 80 µm 282 alloy correlate with the relatively low LCF life of that material. To conclusively establish a causative link between the porosity and the LCF performance, fractographic analysis of the failed LCF specimens was performed.

3.5 | Fractography

SEM micrographs of the fractured surfaces of LCF specimens are shown in Figure 8 for 40 and 80 µm vertically oriented specimens, and in Figure 9 for 40 and 80 µm horizontally oriented specimens. The fractographic examination revealed that fatigue cracks were initiated at or close to the surface for all cases, and propagated transgranularly through the specimen cross-section perpendicular to the loading direction. The final fracture was mixed inter- and transgranular. Similar behavior has been reported for wrought 282 alloy in the literature [23, 41] and can also be observed in Supporting Information Figure S1, which shows the fracture surface of the wrought material.

For the 40 µm vertical sample, multiple initiation points can be seen in Figure 8a,b, however, no defects were found at or near the initiation points. Rather rough morphology of the fracture surface indicates complex crack propagation, starting from multiple initiation points at the sample surface. The transgranular fracture surface can be seen in Figure 8c, as well as two spherical pores, which are typical for the 40 µm 282 alloy, as discussed in section 3.4 above.

The fractured 80 µm vertical sample seen in Figure 8d,e, also showed several initiation points. However, several lack of fusion defects could be observed on the fracture surface, as seen in Figure 8e, which contributed to initiation and acceleration of the crack propagation through the specimen. Large lack of fusion defects were also observed near to the surface - see Figure 8f. These defects have maximum dimensions exceeding 200 µm and sharp features, suggesting they could act as stress concentrators. The observation of feathering marks on the fracture surface adjacent to these defects suggests that these defects acted as crack

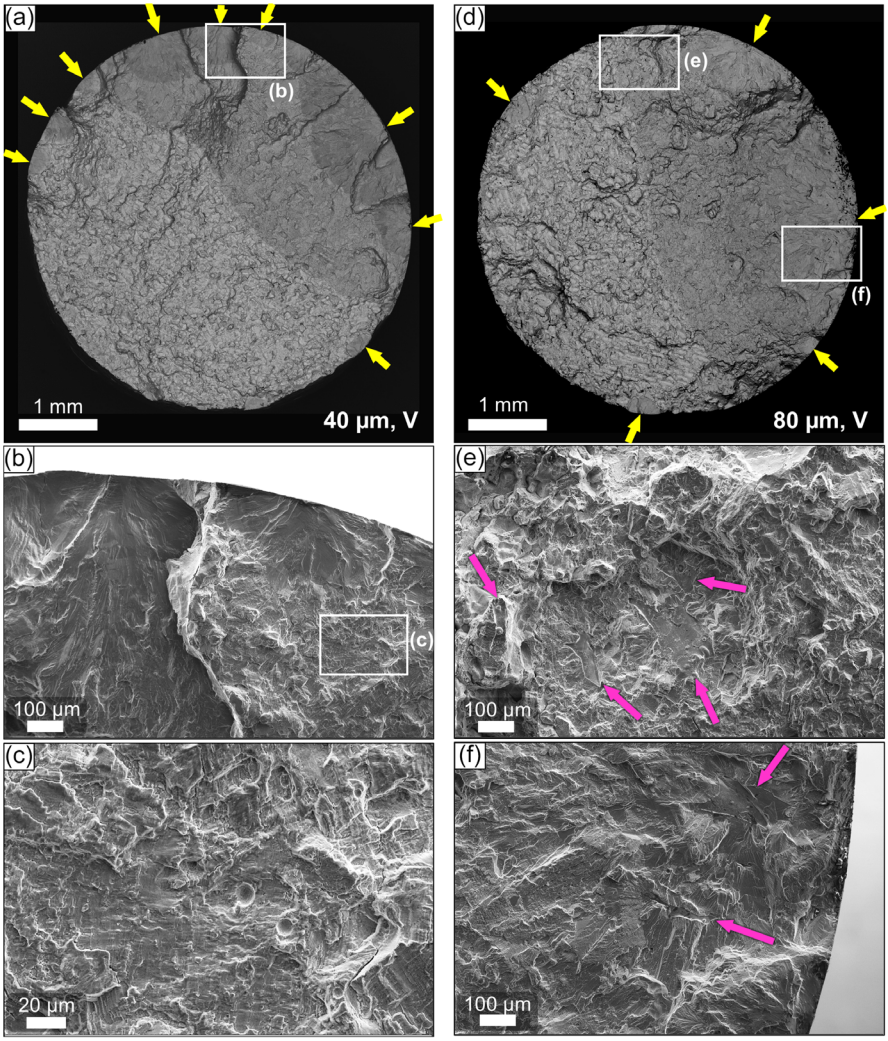

FIGURE 8 | Fracture surfaces of failed vertical LCF specimens from (a) to (c) 40 µm 282 alloy; and (d) to (f) 80 µm 282 alloy. Yellow arrows indicate fatigue crack initiation points, and pink arrows indicate lack of fusion defects.

initiation sites. It is notable that the 80 µm vertically oriented samples showed the lowest LCF life of all conditions.

The fracture surface for a 40 µm horizontally oriented LCF specimen can be seen in Figure 9a–c. Similar to the vertically oriented sample, multiple initiation points at the surface were observed, along with a transgranular fracture surface. No large defects were observed on the fracture surface, nor near the crack initiation points. Conversely, the 80 µm horizontally oriented specimen showed large lack of fusion defects with their major axis oriented perpendicular to the direction of crack growth (parallel to the direction of applied stress) at locations within the specimen bulk. Such defects can be seen in Figure 9e,f. As these defects are not cohesive, they would be expected to negatively impact the fatigue life. However, since they are oriented parallel to the stress axis, their effective cross-sectional area is lower relative to the lack of fusion defects seen in Figure 8f, decreasing their harmful effect on fatigue life. No indications were found that they acted as initiation points in the 80 µm horizontally oriented specimens.

Cross-sections of the failed specimens were examined to further clarify the crack initiation and propagation in different conditions of AM 282. Several large secondary cracks were observed for the specimens in all conditions (see Figure 10) but no correlation of secondary cracks with defects could be found at cross-sections. This suggests that cracks initiated on the surface of specimens from microstructural features, for example, see Figure 10e,f where a crack can be seen initiating on the surface of the wrought specimen from a feature which is probably a twin boundary—an initiation mechanism which is commonly reported in the literature [2, 42]. However, in the cross-section of the failed 80 µm vertical specimen a number of small cracks could be observed around lack of fusion defects oriented perpendicular to the BD (and the axis of applied stress). Some examples of these defects are shown in Figure 11. While these cracks were small relative to the specimen cross-sectional area, their occurrence only in the 80 µm horizontal specimen agrees with the observations from fractography (Figure 8d–f) where lack of fusion defects could be seen on the path of the fatigue crack.

3.6 | Synthesis and Discussion

The above results suggest that while the microstructures of the 40 and 80 µm 282 alloy are very similar, there are clear differences in defects resulting from PBF-LB processing. The fractography results further indicate that the differences in size, morphology,

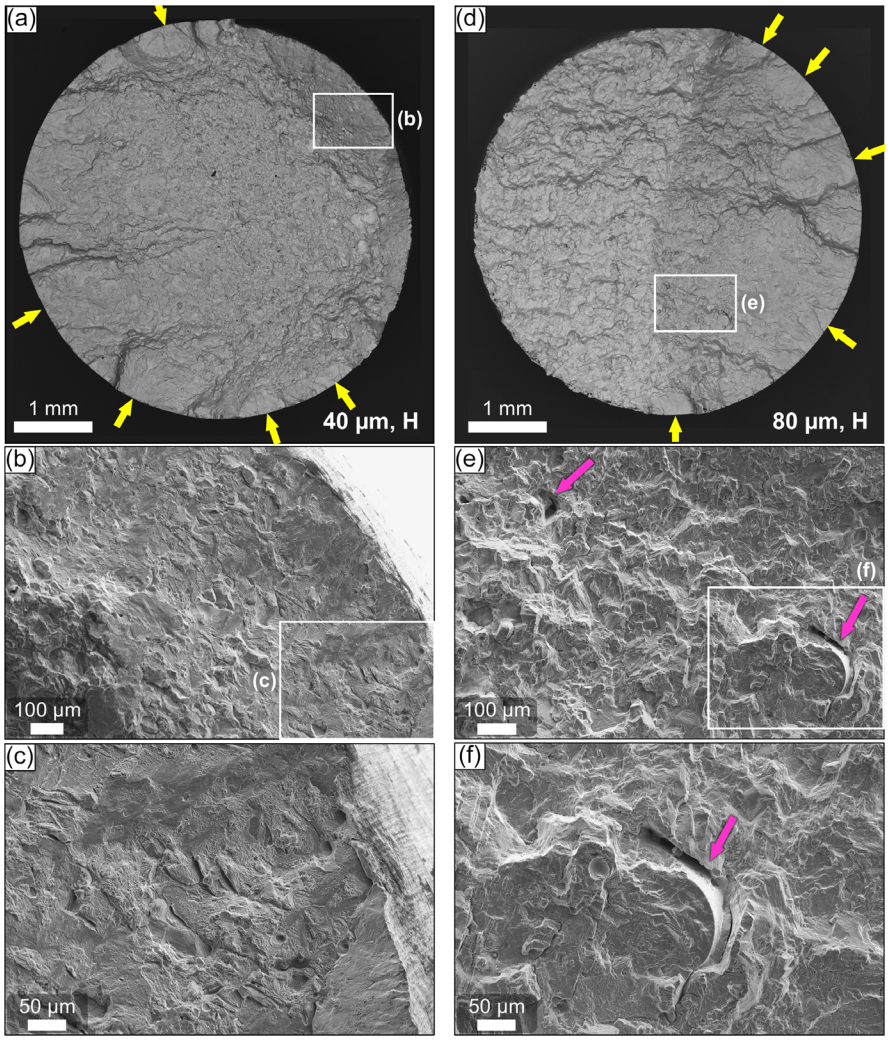

FIGURE 9 | Fracture surfaces of failed horizontal LCF specimens from (a) to (c) 40 µm 282 alloy; and (d) to (f) 80 µm 282 alloy. Yellow arrows indicate fatigue crack initiation points, and pink arrows indicate lack of fusion defects.

and orientation of defects do appear to influence the LCF behavior. In particular, the increased defect fraction in the 80 µm 282 alloy is correlated with the lower fatigue life in the 80 µm LCF specimens.

Fatigue fracture generally progresses in three stages: initiation (stage I), followed by stable propagation of a dominant crack (stage II), and final fracture (stage III) [43, 44]. From the literature on fatigue of AM Ni-base superalloys it is known that crack initiation is the most crucial phase where most of the fatigue life is spent. After cracks are initiated a relatively small number of cycles is required for their propagation, followed by a rapid final fracture [12, 45–47]. Further, it is known that when the material is free from defects, crack initiation occurs mainly from the surface, e.g., from microstructural features such as slip bands or twin boundaries [8, 30, 46, 48, 49]. On the other hand, when defects are present in the material, they may or may not act as fatigue crack initiation sites [8, 12, 46, 49]. This depends on their size, type, morphology, position, and orientation relative to the loading [50].

Considering the results in the light of the literature, the following qualitative explanation for the LCF performance trends between parameters is proposed. In the 40 µm horizontal and vertical specimens, fatigue cracks initiate from the surface due to the lack of any sharp defects or inclusions in the material. Although the material contains defects in the form of spherical pores, no evidence of crack initiation from such pores could be found, which agrees with reports in the literature [1]. Following initiation, fatigue cracks propagate transgranularly until the load-bearing cross-section is sufficiently reduced for final fracture to occur. This behavior, characterized by slow initiation, accounts for the long fatigue life observed in the 40 µm 282 alloy specimens, which is on par with the wrought material. Crack initiation is also slow in the 80 µm horizontal specimens, since the lack of fusion defects in this material are oriented with their long axis parallel to the stress axis and are therefore unlikely to serve as crack initiation sites. However, these large defects do lower the effective load bearing cross-section and therefore accelerate the propagation of the crack (relative to the 40 µm material), which also explains the lower average N_f. The 80 µm vertical specimens contain lack of fusion defects oriented perpendicular to the axis of stress, which effectively act as preincubated cracks. Thus, these specimens see crack initiation both from the surface and from near-surface lack of fusion defects, accelerating the crack initiation stage. Crack propagation is also expected to be fastest in the 80 µm vertical specimens due to the projected

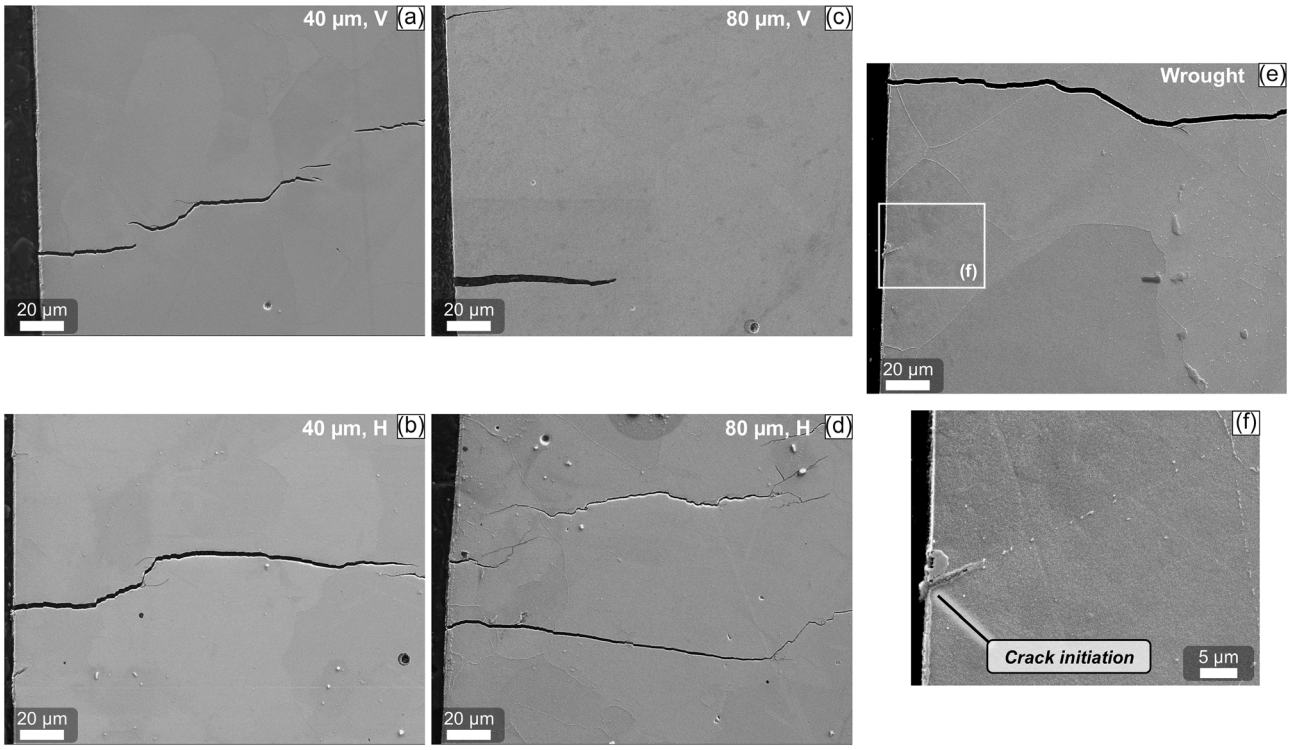

FIGURE 10 | Secondary cracks in cross-sections of failed LCF specimens tested at 760 °C; (a) 40 µm vertical; (b) 40 µm horizontal; (c) 80 µm vertical; (c) 80 µm horizontal; (e) wrought; and (f) suspected crack initiation at twin boundary in failed wrought specimen.

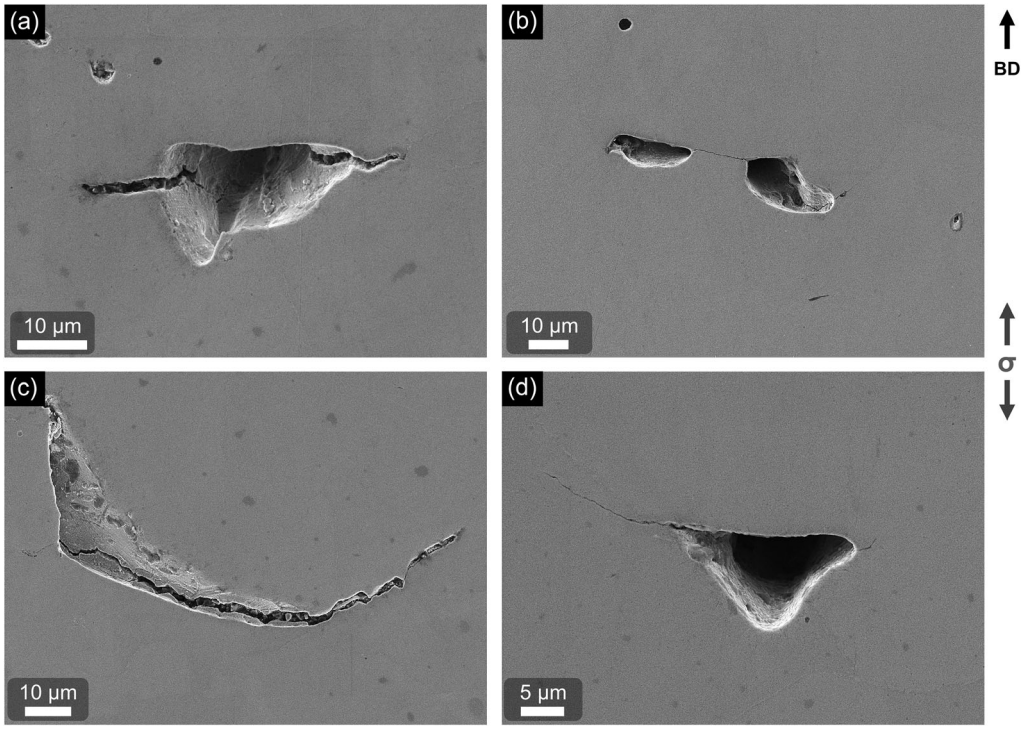

FIGURE 11 | Cracks observed around lack of fusion defects in a cross-section of the failed horizontal 80 µm LCF specimen. Defects (and cracks originating from them) appear to be oriented perpendicular to the axis of applied stress.

area of defects over the load bearing cross-section being maximized due to their orientation. Therefore, both initiation and propagation stages are accelerated in the 80 µm vertical specimens, which accounts for their average N_f being the lowest of all tested conditions. The detrimental effect of lack of fusion defects orientated perpendicular to the loading direction on fatigue life has previously been noted by other researchers as well [50–53].

A result which is not explained by the above discussion is the difference in average N_f between horizontal and vertical 40 µm 282 alloy. A possible explanation could be residual anisotropy which is noted in previous work for AM 282 alloy [21] and has been proposed as the cause for improved fatigue life of vertically oriented specimens [12]. Related trends of better fatigue crack growth resistance in the vertical orientation compared to horizontal have been noted elsewhere in the literature [2, 7, 54]. Further investigations are required to determine the cause of this result. Nevertheless, the anisotropy in fatigue life is an important result and especially worthy of consideration when designing components for AM.

While the 40 µm horizontal, 80 µm vertical, and 80 µm horizontal conditions all showed only small differences in N_f between their respective duplicate specimens, the Wrought condition and 40 µm vertical condition showed wider variation among specimens. However, this level of scatter is a common observance in fatigue testing, and similar variation among specimens can be found in several published reports [8, 29, 34]. According to Sanaei et al., materials with low porosity can be expected to have more scatter in fatigue testing, because the life controlling stage (crack initiation from the surface) has greater randomness, rather than being a function of a known defect population [30]. In addition, the N_f results are validated by reports in the literature for Wrought 282 alloy in fully reversed strain-controlled testing. Pike reported N_f of ≈1300 cycles for 282 alloy sheet at 760°C and 1% total strain range [22], while He et al. reported N_f of ≈2000 cycles for large forgings of 282 alloy tested at 750°C and 0.93% total strain range [23]. These results also indicate that the 40 µm 282 alloy has competitive LCF performance with the Wrought alloy at the tested conditions. Further testing at higher and lower strain ranges and temperatures is needed to better understand the LCF behavior of PBF-LB 282 alloy at a general level.

From a processing perspective, the results show that there remains room for improvement of high-productivity PBF-LB processing to improve density and lower defect fractions. Further process development trials are needed to assess the potential for process improvement without compromising productivity or buildability. Additionally, postprocessing techniques such as hot isostatic pressing, as shown by Herzog et al. [55], are anticipated to be effective in reducing porosity and further improving mechanical properties. These methods may help to further narrow the performance gap between conventional processing and high-productivity parameter sets.

4 | Conclusions

An investigation into the elevated temperature LCF performance of PBF-LB processed 282 alloy was performed, comparing conventional 40 µm layer thickness processing to high-productivity 80 µm process parameters, along with a direct comparison to wrought 282 alloy.

At 760°C with fully reversed loading and 1% total strain range the 40 µm 282 alloy showed the highest fatigue life of $N_f \approx 1700$ cycles in the vertical orientation, and $N_f \approx 1400$ cycles in the horizontal orientation, averaged over 2 specimens. The 80 µm 282 alloy showed lower fatigue life of $N_f \approx 1150$ cycles in the vertical orientation and $N_f \approx 1250$ cycles in the horizontal orientation. The wrought form of the alloy showed average $N_f \approx 1350$ cycles. Metallographic analysis of the 40 and 80 µm 282 alloy conditions showed similar γ-γ' microstructure with carbides at grain boundaries, and generally similar grain structure and grain size. However, high-resolution X-ray CT measurements showed significant differences in porosity resulting from the AM processing parameters, with V_f porosity of 0.036% for the 80 µm but only 0.004% for the 40 µm. Moreover, large and sharp lack of fusion defects were found in the 80 µm material whereas the 40 µm contained only small spherical pores. Failure analysis of the LCF specimens suggests that these lack of fusion defects resulted in faster crack initiation and propagation for the 80 µm 282 alloy relative to the 40 µm, especially in vertically oriented specimens, where the defects were aligned parallel to the direction of fatigue crack propagation.

The results emphasize the criticality of defects in high-performance AM materials subjected to challenging loading conditions, but also highlight the possibility to achieve similar or better performance with respect to wrought material subject to adequate processing parameters.

Acknowledgments

This work was performed in the framework of the Centre for Additive Manufacturing – Metal (CAM^2), financed by Vinnova.

Funding

This study was supported by VINNOVA.

Conflicts of Interest

The authors declare no conflicts of interest.

Data Availability Statement

The data that support the findings of this study are available from the corresponding author upon reasonable request.

References

1. A. Wessman, J. Cormier, F. Hamon, et al., *Microstructure and Mechanical Properties of Additively Manufactured Rene 65, Superalloys*, in, eds. S. Tin, M. Hardy, J. Clews, J. Cormier, Q. Feng, J. Marcin, C. O'Brien, A. Suzuki (Springer International Publishing, 2020), 961–971 https://doi.org/10.1007/978-3-030-51834-9_94.

2. M. M. Kirka, D. A. Greeley, C. Hawkins, and R. R. Dehoff, "Effect of Anisotropy and Texture on the Low Cycle Fatigue Behavior of Inconel 718 Processed via Electron Beam Melting," *International Journal of Fatigue* 105 (2017): 235–243, https://doi.org/10.1016/j.ijfatigue.2017.08.021.

3. C. V. Singh, S. Bagui, B. K. Sahoo, O. S. Umbare, S. Tarafder, and S. Sivaprasad, "Comparison of Low Cycle Fatigue Behaviour of Additively Manufactured and Wrought Inconel 625 Alloys," *Materials Science and Engineering: A* 903 (2024): 146682, https://doi.org/10.1016/j.msea.2024.146682.

4. P. Kanagarajah, F. Brenne, T. Niendorf, and H. J. Maier, "Inconel 939 Processed by Selective Laser Melting: Effect of Microstructure and Temperature on the Mechanical Properties under Static and Cyclic Loading," *Materials Science and Engineering A* 588 (2013): 188–195, https://doi.org/10.1016/j.msea.2013.09.025.

5. M. Kopec, X. Liu, D. Kukla, R. Sitek, and Z. L. Kowalewski, "Effect of Printing Direction on Fatigue Response and Damage Development in Additive Manufactured Haynes 282 Nickel Superalloy," *International*

Journal of Damage Mechanics 34 (2025): 756–770, https://doi.org/10.1177/10567895231204951.

6. A. Bridges, J. Shingledecker, A. Torkaman, and L. Houck, "*Metallurgical Evaluation of an Additively Manufactured Ni-Base Superalloy for Gas Turbine Guide Vanes*," in Proceedings of ASME Turbo Expo 2020, (2020), https://doi.org/10.1115/GT2020-14808.

7. H. R. Javidrad and S. Salemi, "Effect of the Volume Energy Density and Heat Treatment on the Defect, Microstructure, and Hardness of L-PBF Inconel 625," *Metallurgical and Materials Transactions A* 51 (2020): 5880–5891, https://doi.org/10.1007/s11661-020-05992-x.

8. H. Liu, H. Yu, C. Guo, et al., "Review on Fatigue of Additive Manufactured Metallic Alloys: Microstructure, Performance, Enhancement, and Assessment Methods," *Advanced Materials* 36 (2024): e2306570, https://doi.org/10.1002/adma.202306570.

9. S. D. Antolovich, "Microstructural Aspects of Fatigue in Ni-Base Superalloys. Philosophical Transactions of the Royal Society A: Mathematical," *Physical and Engineering Sciences* 373 (2015): 20140128, https://doi.org/10.1098/rsta.2014.0128.

10. A. Pineau and S. D. Antolovich, "High Temperature Fatigue of Nickel-Base Superalloys – A Review with Special Emphasis on Deformation Modes and Oxidation," *Engineering Failure Analysis* 16 (2009): 2668–2697, https://doi.org/10.1016/j.engfailanal.2009.01.010.

11. S. Gribbin, J. Bicknell, L. Jorgensen, I. Tsukrov, and M. Knezevic, "Low Cycle Fatigue Behavior of Direct Metal Laser Sintered Inconel Alloy 718," *International Journal of Fatigue* 93 (2016): 156–167, https://doi.org/10.1016/j.ijfatigue.2016.08.019.

12. E. Sadeghi, P. Karimi, R. Esmaeilizadeh, et al., "A State-of-the-Art Review on Fatigue Performance of Powder Bed Fusion-Built Alloy 718," *Progress in Materials Science* 133 (2023): 101066, https://doi.org/10.1016/j.pmatsci.2022.101066.

13. M. Taghian, M. H. Mosallanejad, E. Lannunziata, G. Del Greco, L. Iuliano, and A. Saboori, "Laser Powder Bed Fusion of Metallic Components: Latest Progress in Productivity, Quality, and Cost Perspectives," *Journal of Materials Research and Technology* 27 (2023): 6484–6500, https://doi.org/10.1016/j.jmrt.2023.11.049.

14. C. Schwerz, F. Schulz, E. Natesan, and L. Nyborg, "Increasing Productivity of Laser Powder Bed Fusion Manufactured Hastelloy X through Modification of Process Parameters," *Journal of Manufacturing Processes* 78 (2022): 231–241, https://doi.org/10.1016/j.jmapro.2022.04.013.

15. R. Gunnerek, "*Increased Productivity of Ferrous Alloys Produced by Powder Bed Fusion - Laser Beam. Licentiate Thesis*," (Gothenburg, Sweden, Gothenburg, Sweden: Chalmers University of Technology, 2024).

16. A. Leicht, M. Fischer, U. Klement, L. Nyborg, and E. Hryha, "Increasing the Productivity of Laser Powder Bed Fusion for Stainless Steel 316L through Increased Layer Thickness," *Journal of Materials Engineering and Performance* 30 (2021): 575–584, https://doi.org/10.1007/s11665-020-05334-3.

17. P. Paradise, D. Patil, N. van Handel, et al., "Improving Productivity in the Laser Powder Bed Fusion of Inconel 718 by Increasing Layer Thickness: Effects on Mechanical Behavior," *Journal of Materials Engineering and Performance* 31 (2022): 6205–6220, https://doi.org/10.1007/s11665-022-06961-8.

18. Y. Murakami, H. Masuo, Y. Tanaka, and M. Nakatani, "Defect Analysis for Additively Manufactured Materials in Fatigue from the Viewpoint of Quality Control and Statistics of Extremes,"*Procedia Structural Integrity* 19 (2019):113–122, https://doi.org/10.1016/j.prostr.2019.12.014.

19. A. S. Shaikh, F. Schulz, K. Minet-Lallemand, and E. Hryha, "Microstructure and Mechanical Properties of Haynes 282 Superalloy Produced by Laser Powder Bed Fusion," *Materials Today Communications* 26 (2021): 102038, https://doi.org/10.1016/j.mtcomm.2021.102038.

20. K. A. Christofidou, H. T. Pang, W. Li, et al., *Microstructural Control and Optimization of Haynes 282 Manufactured Through Laser Powder Bed Fusion, Superalloys 2020*, in eds.S. Tin, M. Hardy, J. Clews, J. Cormier, Q. Feng, J. Marcin, C. O'Brien, A. Suzuki, A. Suzukiu, (Springer International Publishing, 2020) 1014–1023, 2020.

21. A. S. Shaikh, E. Eriksson, M. H. Colliander, K. Minet-Lallemand, and E. Hryha, "Tailored Heat Treatments to Enhance Performance in Additive Manufactured HAYNES 282 Superalloy," *Materialia* 39 (2025): 102334, https://doi.org/10.1016/j.mtla.2025.102334.

22. L. M. Pike, Roger C. Reed, Kenneth A. Green, et al., Development of a Fabricable Gamma Prime Strengthened Superalloy," in *Superalloys 2008 (11th International Symposium)*, eds. Roger C. Reed, Kenneth A Green, Pierre Caron, Gabb Tim, Michael G. Fahrmann, Eric S. Huron, Shiela A. Woodard (2008) 191–200, TMS.

23. J. He, R. Sandström, and S. Notargiacomo, "Low-Cycle Fatigue Properties of a Nickel-Based Superalloy Haynes 282 for Heavy Components," *Journal of Materials Engineering and Performance* 26 (2017): 2257–2263, https://doi.org/10.1007/s11665-017-2586-x.

24. K. Barat, M. Ghosh, S. Sivaprasad, S. K. Kar, and S. Tarafder, "High-Temperature Low-Cycle Fatigue Behavior in HAYNES. 282: Influence of Initial Microstructure," *Metallurgical and Materials Transactions A* 49 (2018): 5211–5226, https://doi.org/10.1007/s11661-018-4760-7.

25. R. Brommesson, M. Ekh, and C. Persson, "Experimental Observations and Modelling of Cyclic and Relaxation Behaviour of the Ni-Based Superalloy Haynes 282," *International Journal of Fatigue* 87 (2016): 180–191, https://doi.org/10.1016/j.ijfatigue.2016.01.027.

26. R. A. Buckson and O. A. Ojo, "Cyclic Deformation Characteristics and Fatigue Crack Growth Behaviour of a Newly Developed Aerospace Superalloy Haynes 282," *Materials Science and Engineering: A* 555 (2012): 63–70, https://doi.org/10.1016/j.msea.2012.06.034.

27. C. Joseph, C. Persson, and M. Hörnqvist Colliander, "Influence of Heat Treatment on the Microstructure and Tensile Properties of Ni-Base Superalloy Haynes 282," *Materials Science and Engineering: A* 679 (2017): 520–530, https://doi.org/10.1016/j.msea.2016.10.048.

28. M. Liu, Y. Cai, Q. Wang, et al., "The Low Cycle Fatigue Property, Damage Mechanism, and Life Prediction of Additively Manufactured Inconel 625: Influence of Temperature," *Fatigue & Fracture of Engineering Materials & Structures* 46 (2023): 3829–3845, https://doi.org/10.1111/ffe.14106.

29. Z. Zhang and Z. Xu, "Fatigue Database of Additively Manufactured Alloys,"*Scientific Data* 10 (2023): 249, https://doi.org/10.1038/s41597-023-02150-x.

30. N. Sanaei and A. Fatemi, "Defects in Additive Manufactured Metals and Their Effect on Fatigue Performance: A State-of-the-Art Review," *Progress in Materials Science* 117 (2021): 100724, https://doi.org/10.1016/j.pmatsci.2020.100724.

31. A. Deshpande, S. Deb Nath, S. Atre, and K. Hsu, "Effect of Post Processing Heat Treatment Routes on Microstructure and Mechanical Property Evolution of Haynes 282 Ni-Based Superalloy Fabricated with Selective Laser Melting (SLM)," *Metals* 10 (2020): 629, https://doi.org/10.3390/met10050629.

32. J. Boswell, J. Jones, N. Barnard, D. Clark, M. Whittaker, and R. Lancaster, "The Effects of Energy Density and Heat Treatment on the Microstructure and Mechanical Properties of Laser Additive Manufactured Haynes 282," *Materials & Design* 205 (2021): 109725, https://doi.org/10.1016/j.matdes.2021.109725.

33. R. Otto, V. Brøtan, P. A. Carvalho, et al., "Roadmap for Additive Manufacturing of HAYNES 282 Superalloy by Laser Beam Powder Bed Fusion (PBF-LB) Technology," *Materials & Design* 204 (2021): 109656, https://doi.org/10.1016/j.matdes.2021.109656.

34. R. Ghiaasiaan, N. Ahmad, P. R. Gradl, S. Shao, and N. Shamsaei, "Additively Manufactured Haynes 282: Effect of Unimodal vs. Bimodal γ'- Microstructure on Mechanical Properties," *Materials Science and*

Engineering: A 831 (2022): 142234, https://doi.org/10.1016/j.msea.2021.142234.

35. H. Zhang, Y. Wang, R. R. de Vecchis, and W. Xiong, "Evolution of Carbide Precipitates in Haynes 282 Superalloy Processed by Wire Arc Additive Manufacturing," *Journal of Materials Processing Technology* 305 (2022): 117597, https://doi.org/10.1016/j.jmatprotec.2022.117597.

36. C. Joseph, C. Persson, and M. Hörnqvist Colliander, "Precipitation Kinetics and Morphology of Grain Boundary Carbides in Ni-Base Superalloy Haynes 282," *Metallurgical and Materials Transactions A* 51 (2020): 6136–6141, https://doi.org/10.1007/s11661-020-06019-1.

37. C. Joseph, M. Thuvander, C. Persson, and M. Hörnqvist Colliander, "Precipitation of γ' during Cooling of Nickel-Base Superalloy Haynes 282," *Philosophical Magazine Letters* 101 (2021): 30–39, https://doi.org/10.1080/09500839.2020.1841314.

38. H. Javidrad, B. Koc, H. Bayraktar, U. Simsek, and K. Gunaydin, "Fatigue Performance of Metal Additive Manufacturing: A Comprehensive Overview," *Virtual and Physical Prototyping* 19 (2024): e2302556, https://doi.org/10.1080/17452759.2024.2302556.

39. R. Gunnerek, Z. Chen, and E. Hryha, "Impact of High-Productivity Process Parameters in Powder Bed Fusion – Laser Beam on Microstructure of Stainless Steel 316L," *European Journal of Materials* 3 (2023): 2292987, https://doi.org/10.1080/26889277.2023.2292987.

40. C. Schwerz, B. A. Bircher, A. Küng, and L. Nyborg, "In-Situ Detection of Stochastic Spatter-Driven Lack of Fusion: Application of Optical Tomography and Validation via Ex-Situ X-Ray Computed Tomography," *Additive Manufacturing* 72 (2023): 103631, https://doi.org/10.1016/j.addma.2023.103631.

41. S. Mukherjee, K. Barat, S. Sivaprasad, S. Tarafder, and S. K. Kar, "Elevated Temperature Low Cycle Fatigue Behaviour of Haynes 282 and Its Correlation with Microstructure – Effect of Ageing Conditions," *Materials Science and Engineering: A* 762 (2019): 138073, https://doi.org/10.1016/j.msea.2019.138073.

42. C. A. Stein, A. Cerrone, T. Ozturk, et al., "Fatigue Crack Initiation, Slip Localization and Twin Boundaries in a Nickel-Based Superalloy," *Current Opinion in Solid State and Materials Science* 18 (2014): 244–252, https://doi.org/10.1016/j.cossms.2014.06.001.

43. M. A. Meyers and K. K. Chawla, *Mechanical Behavior of Materials* (Cambridge University Press, 2012).

44. J. L. González-Velázquez, *Fractography and Failure Analysis* (Springer International Publishing, 2018).

45. T. Lindström, M. Calmunger, R. Eriksson, and D. Leidermark, "Fatigue Behaviour of an Additively Manufactured Ductile Gas Turbine Superalloy," *Theoretical and Applied Fracture Mechanics* 108 (2020): 102604, https://doi.org/10.1016/j.tafmec.2020.102604.

46. N. Martin, A. Hor, E. Copin, P. Lours, and L. Ratsifandrihana, "Impact of Annealing Treatment on the Fatigue Behavior of Inconel 625 Produced by Laser-Based Powder Bed Fusion," *Fatigue & Fracture of Engineering Materials & Structures* 45 (2022):1258–1275, https://doi.org/10.1111/ffe.13648.

47. T. Babinský, I. Šulák, M. Gálíková, I. Kuběna, J. Poloprudský, and L. Náhlík, "Room-Temperature Low-Cycle Fatigue Behaviour of Cast and Additively Manufactured IN939 Superalloy," *Materials Science and Engineering: A* 924 (2025): 147730, https://doi.org/10.1016/j.msea.2024.147730.

48. Klas Solberg, "Fatigue Design for Metallic Components Produced by Additive Manufacturing" (PhD Thesis, Norwegian University of Science and Technology, 2021).

49. A. K. Syed, W. Vesga, B. Dutton, T. Berentshaw, and X. Zhang, "Defect Tolerance and Fatigue Limit Prediction for Laser Powder Bed Fusion Ti6Al4V," *International Journal of Fatigue* 184 (2024): 108285, https://doi.org/10.1016/j.ijfatigue.2024.108285.

50. Y. Nadot, "Fatigue from Defect: Influence of Size, Type, Position, Morphology and Loading," *International Journal of Fatigue* 154 (2022): 106531, https://doi.org/10.1016/j.ijfatigue.2021.106531.

51. J. Doh, N. Raju, N. Raghavan, D. W. Rosen, and S. Kim, "Bayesian Inference-Based Decision of Fatigue Life Model for Metal Additive Manufacturing considering Effects of Build Orientation and Post-Processing," *International Journal of Fatigue* 155 (2022): 106535, https://doi.org/10.1016/j.ijfatigue.2021.106535.

52. R. Molaei and A. Fatemi, "Crack Paths in Additive Manufactured Metallic Materials Subjected to Multiaxial Cyclic Loads including Surface Roughness, HIP, and Notch Effects," *International Journal of Fatigue* 124 (2019): 558–570, https://doi.org/10.1016/j.ijfatigue.2019.03.007.

53. F. Sausto, G. Marchese, E. Bassini, et al., "Anisotropic Mechanical and Fatigue Behaviour of Inconel718 Produced by SLM in LCF and High-Temperature Conditions," *Fatigue & Fracture of Engineering Materials & Structures* 44 (2021): 271–292, https://doi.org/10.1111/ffe.13373.

54. W. Beard, R. Lancaster, N. Barnard, T. Jones, and J. Adams, "The Influence of Surface Finish and Build Orientation on the Low Cycle Fatigue Behaviour of Laser Powder Bed Fused Stainless Steel 316L," *Materials Science and Engineering: A* 864 (2023): 144593, https://doi.org/10.1016/j.msea.2023.144593.

55. D. Herzog, K. Bartsch, and B. Bossen, "Productivity Optimization of Laser Powder Bed Fusion by Hot Isostatic Pressing," *Additive Manufacturing* 36 (2020): 101494, https://doi.org/10.1016/j.addma.2020.101494.

Supporting Information

Additional supporting information can be found online in the Supporting Information section. **Supporting Fig. S1**: Fracture surface of failed LCF specimens from the Wrought alloy. Yellow arrows indicate fatigue crack initiation points. Micrographs in (b) and (c) show final fracture; Micrographs (d) to (f) show fatigue crack. **Supporting Table S1**: Results of ASTM E606 strain-controlled LCF tests at 760°C and strain range of 1.0%.